Journal of Materials Chemistry A

ROYAL SOCIETY OF CHEMISTRY

PAPER

View Article Online
View Journal | View Issue

Cite this: J. Mater. Chem. A, 2025, 13, 25489

A dual-constrained assembly strategy of highly aligned two-dimensional montmorillonite membranes for efficient proton transport†

Zhenlei Wang,[abd] Lianqiu Huang,[a] Lingjie Zhang,*[ab] Tingting Zhang,[c] Jianglin Yan,[a] Licai Chen,[a] Xiongrui Jiang,[a] Damiano Sarocchi,[d] Shaoxian Song,[a] Viridiana García Meza,[b] Mildred Quintana[b] and Yunliang Zhao *[ae]

Driven by the boosted demand for energy storage and conversion devices, highly conductive proton exchange membranes (PEMs) are extremely desired. Assembling atomically thin nanosheets into nanofluidic channels represents one promising way to construct high-performance PEMs. However, how to produce ultra-aligned nanofluidic channels in a universal and scalable manner is still challenging. Here, we report a dual-constrained assembly strategy to fabricate two-dimensional (2D) montmorillonite (MMT) membranes with highly ordered nanochannels and fast proton transport through confined modification with sulfonated polyvinyl alcohol (SPVA). The numerous polar functional groups with rich lone pair electrons of SPVA enabled nanosheets to feature more negative charges and additional proton carriers, improving the spatial orientation degree of nanosheet dispersion *via* the electrostatic confinement effect. The hydrogen bond interaction between SPVA and nanosheets offered a unique capillary force compensation effect to constrain nanochannel disordering during water removal. Consequently, the SPVA-modified MMT membrane presented significantly enhanced alignment of nanochannels, endowing it with ultra-high proton conductivity (134.58 mS cm^{-1}), ultra-low activation energy (9.19 kJ mol^{-1}), and excellent stability. This work provides a facile and general strategy for constructing high-performance PEMs, and opens an avenue for the development and design of highly aligned lamellar membranes.

Received 15th April 2025
Accepted 1st July 2025

DOI: 10.1039/d5ta02997j

rsc.li/materials-a

Introduction

Efficient transport of protons through proton exchange membranes (PEMs) plays a crucial role in biological processes, and energy storage/conversion devices.[1–3] Currently, commercially available PEMs such as Nafion membranes face the great challenge of a severe decline in conductivity and efficiency due to ready dehydration at high temperature and/or low humidity.[4,5] In contrast to amorphous polymers, nanofluidic channels constructed using two-dimensional (2D) nanosheets exhibited excellent stability, and the huge capillary-like force created inside nanochannels can substantially facilitate proton transport, which enables them to be considered as promising candidates for PEMs.[6–8] Notably, the fast proton transport in aqueous systems is usually governed by the Grotthuss mechanism that occurs on the hydrogen bond networks and induces a collective proton motion analogous to a Newton's cradle.[9,10] Such Grotthuss-type proton transport mainly depends on proton bridging of continuous hydrogen bonds, making it important to construct well-aligned nanofluidic channels.[6,11]

The high aspect ratio (*i.e.* the ratio of lateral size to thickness) of nanosheets enables them to spontaneously and preferentially stack face-to-face to form a lamellar nanochannel structure; however, the edge-to-edge interactions between randomly spatially oriented nanosheets in suspension inevitably cause undesirable pre-assembly of 2D building blocks.[12–14] Subsequently, the pre-assembled nanochannels are removed water to enhance the stacking of nanosheets and assemble lamellar membranes.[15] During the assembly process, the capillary forces drive the lateral contraction of nanosheets, resulting in further deterioration of the nanochannel alignment,[16–18] which fails to fully exploit the proton transport potential of the nanofluidic channels of lamellar membranes.

[a]School of Resources and Environmental Engineering, Wuhan University of Technology, Wenzhi Street 34, Wuhan, Hubei 430070, China. E-mail: zhanglj0515@163.com; zyl286@whut.edu.cn

[b]Facultad de Ciencias, Universidad Autonoma de San Luis Potosi, Av. Parque Chapultepec 1570, San Luis Potosi 78210, Mexico

[c]School of Chemical and Environmental Engineering, Wuhan Polytechnic University, Wuhan 430023, China

[d]Instituto de Geologia, Facultad de Ingenieria, Universidad Autonoma de San Luis Potosi, Av. Parque Chapultepec 1570, San Luis Potosi 78210, Mexico

[e]Wuhan Clayene Technology Co., Ltd., Tangxunhu North Road 36, Wuhan, Hubei 430223, China

† Electronic supplementary information (ESI) available. See DOI: https://doi.org/10.1039/d5ta02997j

Therefore, it is imperative to regulate the stacking and assembly behaviors of nanosheets to construct highly aligned and ordered nanofluidic channels for optimizing proton transport in PEMs.

So far, several strategies have been developed to fabricate lamellar membranes with highly aligned nanochannels, which mainly involve: (i) enhancement of the spatial orientation of the nanosheet dispersion,[14,19,20] (ii) optimization of the assembly approaches of nanosheets,[21–23] and (iii) externally assisted nanosheet alignment.[24–26] Based on these strategies, methods such as nanosheet property modulation, shear-induced ordered assembly, chemical cross-linking, and stretch-induced alignment have been developed. While these methods are able to improve the alignment of nanochannels to some extent, they are limited by the complex procedures or their negative effects on ion transport.[27] Tailoring nanosheets to nanofluidic channels with high alignment and rapid proton transport properties through a facile and scalable way is still very challenging.

Herein, we propose a dual-constrained assembly strategy that strengthens the electrostatic confinement effect between nanosheets and offers a capillary force compensation effect to construct highly aligned nanofluidic channels for efficient proton transport. Montmorillonite (MMT), a natural layered silicate mineral, was selected to represent 2D nanomaterials due to its abundant reserves and exceptional stability.[28,29] The exfoliated MMT nanosheets were modified with sulfonated polyvinyl alcohol (SPVA), where SPVA acted as a negatively charged coating, cross-linking agent and proton carrier. Consequently, SPVA-modified MMT (SMMT) nanosheets featured a higher negative charge to enhance the electrostatic repulsion and thereby constrain the edge-to-edge interactions, contributing to the improved spatial orientation degree of the nanosheet dispersion. During the assembly process, the hydrogen bond interaction between SPVA and MMT nanosheets generated tensile forces to compensate for capillary forces, thus restraining nanochannel disordering. Further, SPVA provided additional sulfonic acid groups within the aligned nanochannels to enhance the Grotthuss proton transport mechanism. Benefiting from the dual-constrained assembly strategy, the prepared SMMT membrane presented an ultra-high proton conductivity of 134.58 mS cm^{-1} at 30 °C, ultra-low activation energy of 9.19 kJ mol^{-1}, and outstanding stability. This work provides a universal and scalable strategy for constructing advanced PEMs, which can be extended to the development and design of other aligned 2D lamellar membranes.

Materials and methods

Preparation of SMMT nanosheets and membranes

A dispersion of MMT nanosheets was prepared according to our previous report, including purification, ion exchange and exfoliation.[30] Briefly, the raw MMT mineral was crushed, cleaned and centrifuged at high speed to remove impurities. The resulting MMT suspension was then ion exchanged with NaCl to prepare Na-based MMT and then exfoliated by sonication (output power of 450 W) to obtain MMT nanosheets. Further, sulfonated polyvinyl alcohol (SPVA) equivalent to 15% of the mass of MMT nanosheets was taken and homogeneously mixed with MMT nanosheets for 24 h to obtain SPVA-modified SMMT nanosheets, and the details of the preparation of SPVA are described in ESI Text S3.†

MMT and SMMT membranes were assembled by vacuum filtration of the nanosheet dispersion using a PES filter (4.0 mm diameter, 0.02 μm pore size, Whatman). The MMT membrane was easily peeled off from the filter membrane after natural air drying. The obtained MMT membrane was white and translucent, and could be easily cut into the required shapes using a razor blade. Large scale membranes were prepared using a PES filter of 10 mm diameter.

Preparation of the nanofluidic devices

The MMT and SMMT membranes were cut into rectangular pieces and immersed into a mixture of polydimethylsiloxane (PDMS) and curing agent to cure. Two reservoirs were excavated in the area at the ends of the membrane to expose the membrane to the electrolyte solutions. Before each test, the conduit device was immersed in a certain concentration of electrolyte for 24 h to ensure full hydration of the nanochannels. Two Ag/AgCl electrodes used as the working electrode and reference electrode were inserted into the source and drain reservoirs to measure the ionic current of the MMT conduits at different electrolyte concentrations.

Conductivity measurement of membranes

The proton conductivity of membranes was determined based on *I–V* tests. Specifically, the linear scan voltammetry (LSV) method was applied to measure the *I–V* curves of proton transport through nanochannels in a scanning voltage range from −0.5 V to 0.5 V with the scanning rate of 0.01 V s^{-1}. The ionic conductivity (σ, S cm^{-1}) of the membrane at different electrolyte concentrations could be calculated according to the following equation:

$$\sigma = Kl/wh \quad (1)$$

where l (cm), w (cm), and h (cm) are the length, width and height of the MMT channel, respectively. K refers to the slope of the *I–V* curves.

The activation energy (E_a) values for the MMT and SMMT membranes were obtained by least squares fitting of the Arrhenius diagram.[6] E_a was calculated using eqn (2):†

$$\sigma = \frac{\sigma_0}{T}\exp\left(\frac{-E_a}{kT}\right) \quad (2)$$

where σ_0 stands for the preexponential factor; k and T are the Boltzmann constant and the absolute temperature in kelvin, respectively.

Results and discussion

Preparation of the spatially ordered SMMT nanosheets

The fabrication procedure of the well-aligned SMMT membrane is shown in Fig. 1a. The MMT nanosheets were first produced

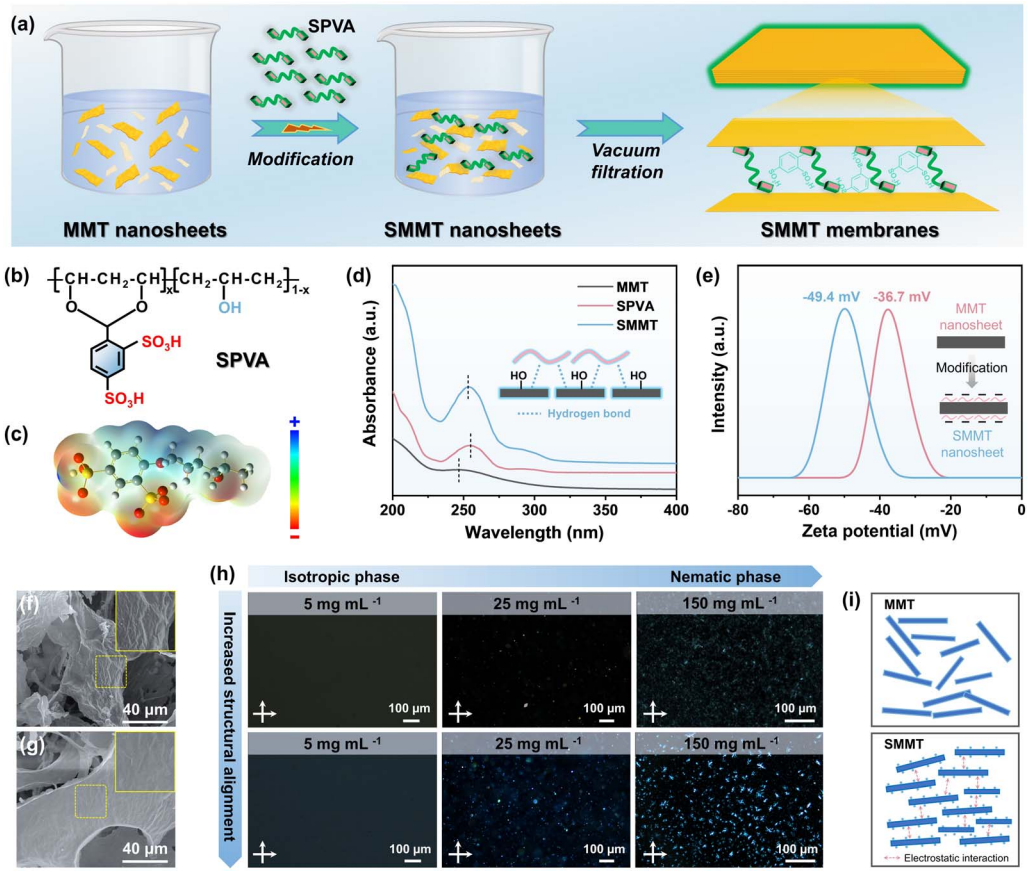

Fig. 1 (a) Schematic illustration of the preparation process of the SMMT membrane. (b) Molecular structure and (c) electrostatic potential of the SPVA molecule. (d) UV-vis absorption spectra of the SPVA solution, MMT nanosheet, and SMMT nanosheet. (e) Zeta potential of MMT nanosheets before and after SPVA modification. SEM images of (f) MMT nanosheets and (g) SMMT nanosheets after liquid nitrogen transient freeze-drying treatment. (h) POM images of MMT and SMMT nanosheets in dispersions with different concentrations. (i) Schematic illustration of the effect of SPVA modification on the spatial distribution of nanosheets in dispersions.

through ultrasound-assisted exfoliation. The atomic force microscopy (AFM) image of MMT nanosheets revealed typical monolayer morphology with an average lateral size of 220 nm and thickness of 1.5 nm (Fig. S1†). The as-prepared nanosheet colloidal solution presented a homogeneous dispersion (Fig. S2†). Further, the sulfonated SMMT nanosheets were obtained by physically blending MMT with the aqueous solution of sulfonated poly(vinyl alcohol) (SPVA), which is an ideal hydrogen-bonding agent and proton carrier due to its numerous oxygen-containing polar groups (Fig. 1b).[31] The detailed synthesis of SPVA is described in Text S3 and Fig. S3 in the ESI.† As MMT nanosheets are mixed with the SPVA solution, SPVA molecules readily coat onto the MMT surface *via* hydrogen bonds, causing sandwich-structured nanosheets.[17,32] This was revealed by UV-vis absorption spectra, where the peaks corresponding to MMT and SPVA were significantly shifted and integrated into a new peak after mixing, suggesting hydrogen bond interaction between the hydroxyl groups of MMT and sulfonic acid groups (Fig. 1d).[33] Such interaction was further verified by the blue shift of X-ray photoelectron spectroscopy (XPS) spectra for the O 1s core level (Fig. S4†). After sulfonation modification, the zeta potential of the nanosheets shifted from −36.7 mV to −49.4 mV, which also provided further proof for the coating of SPVA on the MMT surface (Fig. 1e). The molecular structure of SPVA includes numerous polar functional groups (*i.e.*, –OH and –SO_3H) with rich lone pair electrons, featuring a negative electrostatic potential (ESP), which enhanced the negative charge of MMT nanosheets (Fig. 1c).

As expected, the dramatic change in the surface potential of nanosheets is likely to affect their spatial arrangement. We investigated the spatial microstructure of MMT and SMMT nanosheets in colloidal solutions using liquid nitrogen transient freeze-drying technology (for details, see ESI Text S4†). The scanning electron microscopy (SEM) images demonstrated the chaotic waviness and wrinkles in MMT nanosheets, suggesting that MMT had a randomly spatial orientation degree in the suspension, which readily induced the edge-to-edge interactions between nanosheets,[13] resulting in edge overlapping and self-folding (Fig. 1f). In contrast, SMMT exhibited a markedly flatter morphology with less wrinkles, which revealed the higher spatial orientation degree of SMMT nanosheets in the suspension after sulfonation (Fig. 1g). Further, we also experimentally identified the spatial arrangement of nanosheet dispersions by polarized optical microscopy (POM). As shown in Fig. 1h, the birefringence of both nanosheets became more distinct as the concentration of the suspension increased, indicating the

transition of the nanosheets from the isotropic to the nematic phase.[19] It is noteworthy that the birefringence of SMMT nanosheets was significantly stronger than that of MMT at the same concentration, proving that the SPVA coating of MMT improved the arrangement of nanosheets in the suspension. This might be ascribed to that the higher negative charge of nanosheets originating from negatively charged SPVA generates an electrostatic confinement effect, which constrained the random dispersion and engagement of nanosheets driven by the edge-to-edge interaction between nanosheets.[34] As a result, SMMT nanosheets presented a more stable and ordered dispersion in the suspension, favoring the aligned stacking and assembly of nanosheets into 2D lamellar membranes (Fig. 1i).

Fabrication of the in-plane aligned SMMT membrane

MMT and SMMT nanosheets were readily self-assembled into lamellar membranes with nanofluidic channels by vacuum filtration (Fig. 1a), which were self-supporting and flexible (Fig. S5†). The three-dimensional AFM images presented visually the topographical differences between MMT and SMMT membranes, where the latter had arithmetic mean roughness (R_a) as low as 10.7 nm, far lower than that of the former membrane with a R_a of 45.7 nm (Fig. 2a and b). This was verified by the increased water contact angle of the SMMT membrane surface (Fig. S6†). Furthermore, the SEM images showed that the SMMT membrane featured a smoother surface with less wrinkles compared to the MMT membrane (Fig. 2c and d). The cross-sectional images revealed that the higher alignment of the SMMT membrane with ordered nanochannels originated from the layer-by-layer stacking of SMMT nanosheets, and SPVA was uniformly distributed in the membrane, while the twisted wrinkles in the MMT membrane suggested the disordered stacking of nanosheets (Fig. 2e, f, S7 and S8†). Moreover, the microstructure of the nanochannels was analyzed usingX-ray diffraction (XRD) patterns of the membranes (Fig. 2g). It can be found that compared to the MMT membrane, the SMMT membrane showed a narrower and stronger peak corresponding to the (001) plane, demonstrating more ordered nanochannels. In addition, the nanochannel size of the SMMT membrane was expanded from 0.29 nm to 0.34 nm (d-spacing of the SMMT membrane ≈13.0 Å, platelet thickness of MMT ≈9.60 Å, namely, the interlayer free spacing ≈3.40 Å), which was caused by the SPVA coated on the MMT nanosheets being intercalated into the nanochannels as the assembly process proceeded.[35] Such expanded nanochannels were proved by the transmission electron microscopy (TEM) images of the membranes, in which the lattice spacing of the SMMT membrane assigned to the (001) plane increased from 1.252 to 1.295 nm (Fig. S9†). Further, combining with the XPS spectra for the S 2p and O 1s core levels, the hydrogen bond interaction between intercalated SPVA and MMT nanosheets was demonstrated (Fig. S10 and S11†).

Further, we applied POM and wide-angle X-ray diffraction (WAXD) to determine the stacking orientation of nanosheets in the membranes. As shown in Fig. S12,† the MMT membrane exhibited a distributed hue with a dispersion degree of 31.87°, indicating poorly aligned nanosheets. By contrast, the SMMT nanosheets showed good in-plane stacking behavior in membranes according to the uniform hue over hundreds of micrometers and low dispersion degree (15.59°) of the POM image. The orientation degree of nanosheets in the membranes was quantitatively analyzed *via* WAXS patterns. From 2D patterns, the SMMT membrane presented a more concentrated and intensive scattering compared to that of the MMT membrane, indicating the higher in-plane alignment of

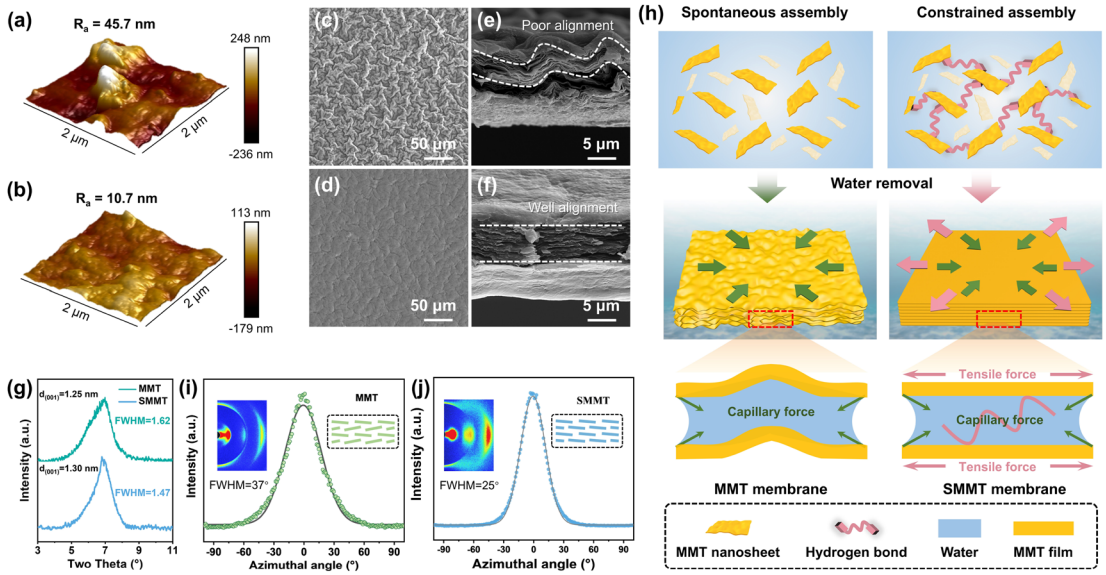

Fig. 2 Three-dimensional AFM images of (a) MMT and (b) SMMT membranes. Surface SEM images of (c) MMT and (d) SMMT membranes. Cross-sectional SEM images of (e) MMT and (f) SMMT membranes. (g) XRD patterns of MMT and SMMT membranes. WAXD patterns of (h) MMT and (i) SMMT membranes. (j) Schematic illustration of the hydrogen bonding interaction between interlayer SPVA and MMT nanosheets to generate tensile forces for compensating the capillary forces during water removal.

nanosheets (Fig. 2h and i). Furthermore, the WAXD data were converted into 1D azimuthal plots. The SMMT membrane (33°) had a narrower full width at half maximum (FWHM) than the MMT membrane (37°), revealing that SPVA modification of MMT can effectively improve the nanosheet alignment. Also, we quantified the planar orientation degree of nanosheets in membranes through Herman's orientation factor (for details, see the ESI†). The orientation factor was increased from 0.671 to 0.854 after modification (Fig. S13†). Such enhanced in-plane orientation of SMMT nanosheets illustrated the highly aligned and continuous nanochannels of the SMMT membrane.

The significantly improved alignment of the membrane and nanochannel structure due to our dual-constrained assembly strategy could be attributed to two reasons: (i) the higher spatial orientation degree of the SPVA-modified nanosheets allows for more aligned pre-assembly (Fig. 1f–i); (ii) during the water removal of the pre-assembled network to induce stacking of nanosheets, the capillary force drives the lateral contraction of nanosheets, leading to the change of the formed nanochannels from flat to wavy.[15] Meanwhile, the hydrogen bond interaction between interlayer SPVA and MMT nanosheets exerts tensile forces to compensate for the capillary forces, thus restraining the disordering of the nanochannels (Fig. 2j).[17] The high alignment of the SMMT membrane is capable of facilitating proton transport.

Proton conductivity of the SMMT membrane

To measure the proton conductivity of the as-obtained membranes, we prepared a homemade nanofluidic device (Fig. S14†), in which the MMT membranes were embedded in a PDMS elastomer with their ends exposed to the HCl solution (Fig. 3a). To avoid inadequate hydration of the MMT nanochannels (Fig. S15†) and ensure stable proton conductance tests, the membranes were wetted in HCl for 24 h prior to procedures. The representative current–voltage (I–V) curves of the MMT and SMMT membranes were determined in 0.1 M HCl solution (Fig. S16 and S17†). The conductance (G) was then calculated from the slope of the I–V curve, and the proton conductivity (σ) was determined based on the dimensions of the 2D nanochannel. Fig. 3b presents the temperature-dependent proton conductivity through the membranes. Both MMT and SMMT membranes showed a pronounced increase in

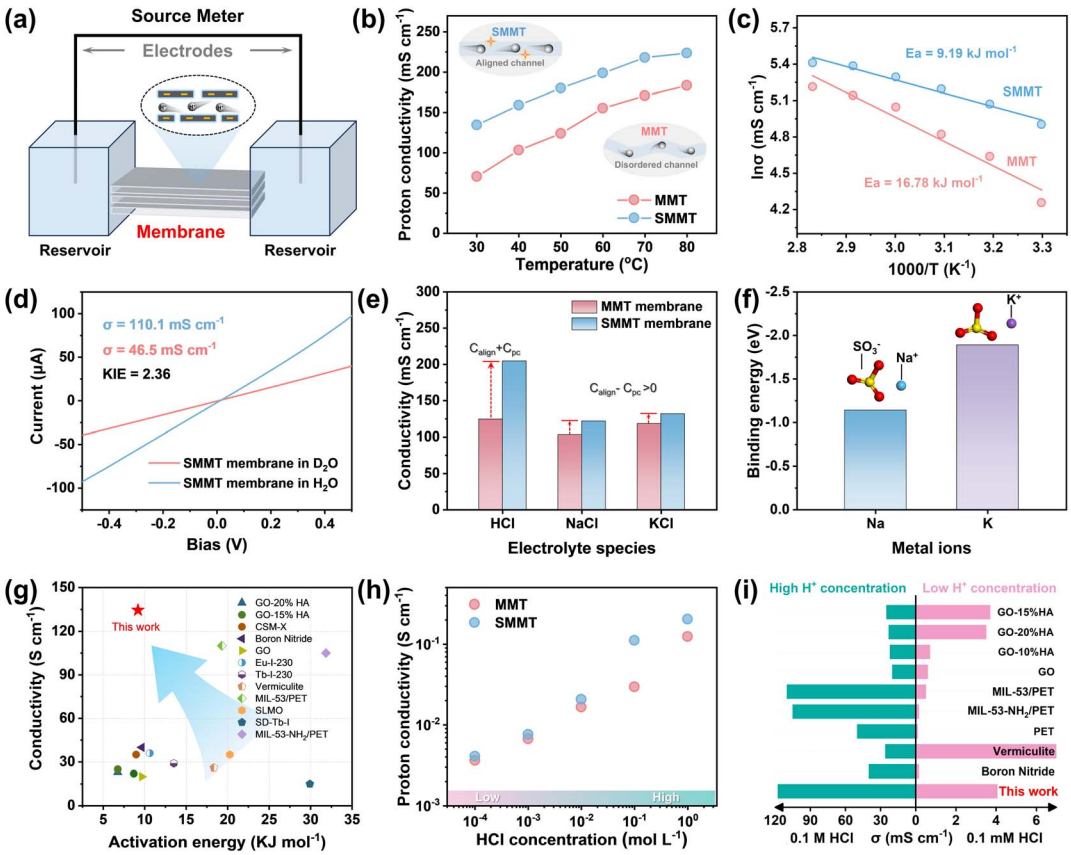

Fig. 3 (a) Schematic illustration of the nanofluidic device. (b) Temperature-dependent proton conductivities and (c) Arrhenius plots of the MMT and SMMT membranes. (d) The I/V curves of the MMT and SMMT membranes recorded in HCl–D_2O and HCl–H_2O solutions of 0.1 M at room temperature. (e) The conductivities of MMT and SMMT membranes in different electrolytes of 1 M. (f) The binding energies between Na^+/K^+ and SO_3^-. (g) Proton conductivity and activation energy of the SMMT membrane compared with those of state-of-the-art PEMs reported in the literature (for details, see ESI Table S1†). (h) Concentration-dependent proton conductivities of the MMT and SMMT membranes at room temperature. (i) Proton conductivities of the SMMT membrane at low (0.1 mM) and high (0.1 M) proton concentrations compared with those of state-of-the-art PEMs reported in the literature (for details, see ESI Table S2†).

conductivity with increasing temperature from 30 °C to 80 °C due to the thermally activated behavior of proton transport. Obviously, the proton conductivity of SMMT was significantly higher than that of MMT. In particular, the conductivity of SMMT at 30 °C was as high as 134.58 mS cm^{-1}, which showed an increase of 91.19% compared to MMT (70.39 mS cm^{-1}).

We further explored the mechanism of proton transport in membranes based on the Arrhenius analysis (Fig. 3c). The activation energies (E_a) were estimated to be 16.78 and 9.19 kJ mol^{-1} for the MMT and SMMT membranes, respectively, which were below 40 kJ mol^{-1}, suggesting that proton transport in the membranes followed the Grotthuss transport mechanism.[36] Furthermore, we carried out the kinetic isotope effect (KIE) measurement of the SMMT membranes by soaking the devices in deuterated electrolyte solution to exchange H^+ with D^+. For the Grotthuss mechanism, the KIE value is required to exceed $(m_D/m_H)^{1/2} \sim 1.4$ since the mass of the D atom (m_D) is twice that of the H atom (m_H).[6] In contrast, the KIE value for the vehicle mechanism is equal to the mass ratio of D_2O to H_2O, *i.e.*, ~1.2. As exhibited in Fig. 3d, the conductivity of the SMMT membrane in the H_2O system was 2.36 times higher than that in the D_2O system, providing solid proof for the proton transport governed by the Grotthuss mechanism. It is noted that the E_a of proton transport greatly reduced from 16.78 to 9.19 kJ mol^{-1} after SPVA modification, which also confirmed the enhanced proton transport in the SMMT membrane.

The improvement in proton transport might stem from two aspects: (i) the nanosheets modified with SPVA feature good spatial orientation and preferential planar alignment in membranes, enabling more ordered nanochannels for proton transport. Based on the Nernst–Einstein relationship ($\sigma = Fa\mu$, where F is Faraday's constant, a refers to ion concentration and μ represents the effective mobility of ions), the enhanced alignment of nanochannels and thereby improved effective mobility of protons is able to facilitate proton conductivity.[37] (ii) SPVA with $-SO_3H$ groups can provide additional proton carriers to create rich hydrogen bond networks for accelerating proton transport. To this end, we determined the ion exchange capacity (IEC) of membranes before and after modification with SPVA (Fig. S18†). It was found that the SMMT showed an increased IEC value compared to MMT, demonstrating the successful introduction of $-SO_3H$ groups. Notably, there was an increase in IEC of only 18.5% due to the low SPVA addition, making it hard for such a limited number of proton carriers to deliver a large increase in proton conductivity. As exhibited in the thermogravimetric analysis (TGA), compared to the pristine MMT membrane, an additional slight weight loss (6.06%) occurred at around 270 °C, corresponding to the decomposition of the SPVA, which affirmed the successful introduction of $-SO_3H$ groups but in small amounts (Fig. S19†). Therefore, it can be concluded that the enhanced proton conductivity of the SMMT membrane mainly depended on the increased orientation degree of nanochannels due to the electrostatic confinement effect (Fig. 1i) and capillary force compensation effect (Fig. 2h) of SPVA, while additional proton carriers played a subsidiary role.

Further, we measured the conductivities of Na^+ and K^+ in MMT and SMMT membranes to determine the contributions of channel alignment (C_{align}) and proton carriers (C_c) of SPVA to proton conductivity (Fig. 3e). Specifically, the transport of Na^+ and K^+ in membranes obeys the vehicle mechanism, which requires a highly aligned channel structure.[38] The SPVA has a negative C_c on Na^+ and K^+ transport in membranes due to the stronger binding interaction between $-SO_3H$ groups and cations (Fig. 3f). Unexpectedly, the Na^+ and K^+ conductivities of the SMMT membrane were higher than those of the MMT membrane, revealing the dominant effect of C_{align} in ion transport. In contrast, protons, in addition to the vehicle mechanism for diffusion and migration, mainly undergo hopping transport *via* the Grotthuss mechanism.[39] As a strong acid, the $-SO_3H$ groups can bind to protons released from hydrated hydrogen ions or free protons, and then dissociate to facilitate proton hopping transport. Thus, SPVA imparts a positive C_c to the SMMT membrane. Accordingly, the increased orientation degree of nanochannels and additional proton carriers jointly contributed to rapid proton conduction, where the former holds the primary role. Benefiting from these properties, the SMMT membrane exhibited low E_a and high conductivity, outperforming most of the state-of-the-art PEMs reported in the literature under similar conditions (Fig. 3g).

The concentration-dependent proton conductivity of MMT and SMMT membranes was demonstrated as well (Fig. S20†). As displayed in Fig. 3h, with increasing concentration, the conductivity of both membranes significantly increased, which indicated that MMT-based membranes are capable of offering outstanding proton conductivity through 2D nanochannels once enough protons are available. As expected, SMMT with highly ordered nanochannels presented obviously enhanced conductivity under the tested conditions. Furthermore, we compared the proton conductivity at low (0.1 mM) and high (0.1 M) proton concentrations with that of the reported PEMs in the literature (Fig. 3i). The results demonstrated the universal high-performance of the SMMT membrane, revealing the advancement of our dual-constrained assembly strategy in achieving fast proton transport.

Conductivity properties of the SMMT membrane

Stability is a common challenge for PEMs in practical applications in complex environments. Therefore, the stability of proton conductivity of the SMMT membrane was investigated comprehensively. It was found that the SMMT membrane remained stable after 30 days of immersion in 0.1 M HCl solution, demonstrating hydro-stability (Fig. S21†). The dimensional stability of the SMMT membrane was also confirmed by the negligible in-plane (<3.2%) and through-plane (<5.0%) dimensional swelling at various temperatures at a saturated relative humidity of 98% (Fig. S22†). Furthermore, the conductivity of the SMMT membrane could remain constant during a continuous long-term operation for nearly 1000 min under both room and high temperatures with negligible structural changes, indicating the admirable stability (Fig. 4a and S23–S25†). Such thermal stability was further

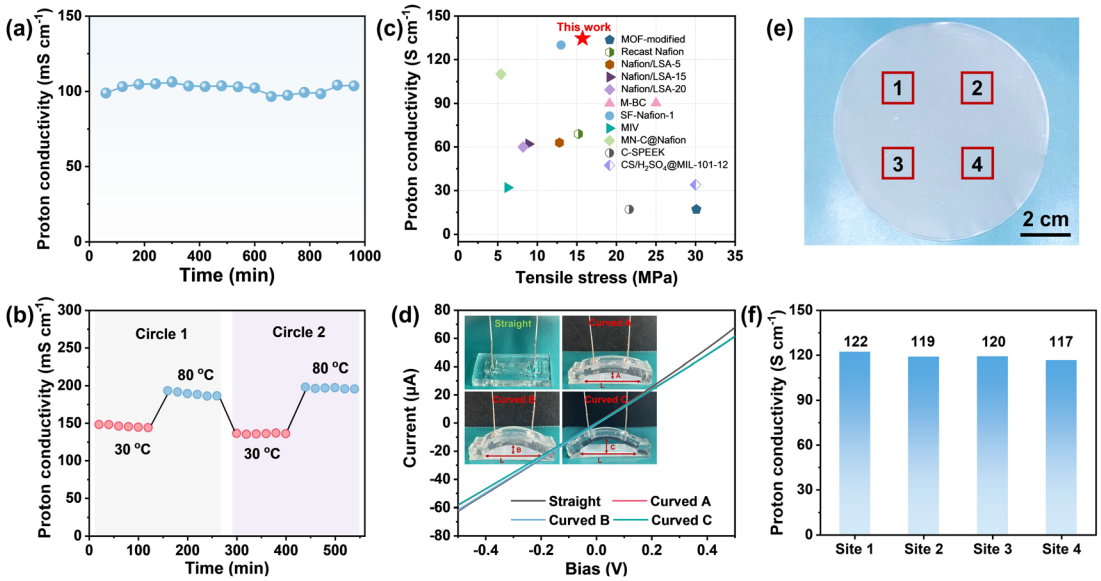

Fig. 4 (a) Proton conductivity stability of the SMMT membrane during the long-term test at room temperature. (b) Proton conductivity stability of the SMMT membrane during two heating–cooling cycles from 30 to 80 °C. (c) Proton conductivity and mechanical strength of the SMMT membrane compared with those of state-of-the-art PEMs reported in the literature (for details, see ESI Table S3†). (d) Representative *I*–*V* curves of the SMMT membrane recorded at 0.1 M HCl concentration at the straight and different curved states. The inset shows the photographs of the SMMT nanofluidic device at curved and straight states. (e) The photograph of the scaled-up free-standing SMMT membrane marked with four randomly selected test sites. (f) Proton conductivities at different sites of the scaled-up SMMT membrane.

confirmed by the low and slow weight loss on heating to 250 °C, which is the typical highest working temperature for PEMs (Fig. S19†). Also, the SMMT membrane presented high tolerance during successive cooling–heating cycles from 30 to 80 °C. The conductivity did not exhibit a decline at each cooling–heating cycle, which could be assigned to the intrinsic structural stability of nanochannels assembled by 2D nanoclays (Fig. 4b).

Mechanical performance, another critical property for PEMs, was evaluated by stress–strain curves (Fig. S26†). Due to the poorly aligned stacking and arrangement of nanosheets in the MMT membrane, which reduced the inter-nanosheet stress transfer efficiency and caused local stress concentration, the MMT membrane had limited mechanical strength (3.61 MPa).[40] In the case of the SMMT membrane, however, Young's modulus (813 MPa) and tensile strength (15.72 MPa) were significantly improved owing to the more ordered stacking of the SMMT nanosheets and the inter-nanosheet bonding of hydrogen bonds. Compared with the PEMs reported in the literature, the SMMT membrane showed outstanding proton conduction and mechanical stability (Fig. 4c). Further, the flexibility of the SMMT membrane was assessed. The membrane could maintain structural integrity after hundreds of bending cycles. We determined the proton conductivity of the curved SMMT membrane by bending the nanofluidic device to varying degrees (Fig. 4d). It was found that the *I*–*V* curves recorded in the curved and straightened states almost overlapped, that is, the conductivity remained constant, which confirmed the robust nanochannels of the SMMT membrane for proton transport.

To explored the reversibility of the scaled-up membranes, we prepared two SMMT membranes with a diameter of 10 cm. Then, each membrane was divided into nine regions for measuring the thickness (Fig. S27†). It was displayed that all regions in both membranes had almost the same thickness (~18 μm), illustrating that the scale-up of the SMMT membranes had good consistency and reversibility (Fig. S28†). In addition, we randomly selected four sites for performing proton transport (Fig. 4e). As displayed in Fig. 4f, the conductivities of the four sites were in good agreement, proving the excellent homogeneity of the SMMT membranes. It was noted that the size and thickness of the membrane could be flexibly tailored by controlling the preparation process and the amount of nanosheets, presenting the promise of simple large-scale manufacture in the future.

Conclusions

In summary, to address the vulnerability of nanochannels to disorder during the construction of 2D lamellar PEMs, we developed a dual-constrained assembly strategy to induce the ordered stacking and assembly of nanosheets into aligned nanofluidic channels. Characterizations and experiments revealed that through facile modification with SPVA, MMT nanosheets were endowed with more negative charges and additional proton carriers, which created an electrostatic confinement effect to constrain the edge-to-edge interaction between nanosheets for a more stable and ordered dispersion. Further, the hydrogen bond interaction between SPVA and nanosheets offered in-plane tensile forces to constrain nanochannel disordering driven by capillary forces. Benefiting from these emerging properties, the SPVA-modified MMT membrane exhibited greatly increased alignment, thereby dramatically

increasing the proton conductivity by 91.19% and lowering the energy barrier of proton transport by 82.5%, compared to the pristine MMT membranes. In addition, the SMMT membrane featured excellent stability and scalability as well. Compared with other assembly strategies, our dual-constrained assembly strategy presented the advantages of universality, accessibility and sustainability in constructing high-performance PEMs with highly ordered nanochannels, which can be expended for the development of different lamellar membrane fields.

Data availability

Data supporting the findings of this work are presented in the paper and its ESI.† All data included in this work are available from the corresponding authors upon request.

Author contributions

Zhenlei Wang: investigation, data curation, methodology, software, visualization, writing – original draft. Lianqiu Huang: formal analysis, investigation. Lingjie Zhang: conceptualization, methodology, software, visualization, writing – original draft, writing – review & editing. Tingting Zhang: resources, project administration. Jianglin Yan: methodology, validation. Licai Chen: investigation, methodology. Xiongrui Jiang: methodology. Damiano Sarocchi: supervision. Shaoxian Song: resources, supervision. Viridiana García Meza: investigation. Mildred Quintana: validation, project administration, resources, supervision, writing – review & editing. Yunliang Zhao: conceptualization, funding acquisition, project administration, resources, supervision, writing – review & editing.

Conflicts of interest

There are no conflicts to declare.

Acknowledgements

The financial support for this work from the National Natural Science Foundation of China (52374275), Natural Science Foundation of Hubei Province of China (2023AFA084), and National Key R&D Program of China (2022YFC2906300) is gratefully acknowledged. Zhenlei Wang would like to thank CONAHCYT for granting him a scholarship (No. 1327527) during his PhD study.

References

1 K. Jiao, J. Xuan, Q. Du, Z. Bao, B. Xie, B. Wang, Y. Zhao, L. Fan, H. Wang, Z. Hou, S. Huo, N. P. Brandon, Y. Yin and M. D. Guiver, *Nature*, 2021, **595**, 361–369.
2 J. R. Schnell and J. J. Chou, *Nature*, 2008, **451**, 591–595.
3 B. Shi, X. Pang, B. Lyu, H. Wu, J. Shen, J. Guan, X. Wang, C. Fan, L. Cao, T. Zhu, Y. Kong, Y. Liu and Z. Jiang, *Adv. Mater.*, 2023, **35**, 2211004.
4 C. Wang, Y. Shen, X. Wang, Y. Zhang, C. Wang, Q. Wang, H. Li, S. Wang and D. Gui, *ACS Appl. Mater. Interfaces*, 2024, **16**, 22648–22656.
5 X.-J. Cao, L.-H. Cao, X.-T. Bai, X.-Y. Hou and H.-Y. Li, *Adv. Funct. Mater.*, 2024, **34**, 2409359.
6 X. Qian, L. Chen, L. Yin, Z. Liu, S. Pei, F. Li, G. Hou, S. Chen, L. Song, K. H. Thebo, H.-M. Cheng and W. Ren, *Science*, 2020, **370**, 596–600.
7 R. R. Nair, H. A. Wu, P. N. Jayaram, I. V. Grigorieva and A. K. Geim, *Science*, 2012, **335**, 442–444.
8 C. Chen, J. Chen, Y. Peng, M. Wang, D. Luo, Y. Li, R. S. Ruoff and S. H. Lee, *Matter*, 2024, **7**, 1259–1274.
9 C. T. Wolke, J. A. Fournier, L. C. Dzugan, M. R. Fagiani, T. T. Odbadrakh, H. Knorke, K. D. Jordan, A. B. McCoy, K. R. Asmis and M. A. Johnson, *Science*, 2016, **354**, 1131–1135.
10 B. Shi, X. Pang, S. Li, H. Wu, J. Shen, X. Wang, C. Fan, L. Cao, T. Zhu, M. Qiu, Z. Yin, Y. Kong, Y. Liu, M. Zhang, Y. Liu, F. Pan and Z. Jiang, *Nat. Commun.*, 2022, **13**, 6666.
11 Z. Zhang, L. Liang, J. Feng, G. Hou and W. Ren, *Nat. Commun.*, 2024, **15**, 2706.
12 X. Lu, U. R. Gabinet, C. L. Ritt, X. Feng, A. Deshmukh, K. Kawabata, M. Kaneda, S. M. Hashmi, C. O. Osuji and M. Elimelech, *Environ. Sci. Technol.*, 2020, **54**, 9640–9651.
13 X. Shen, X. Lin, N. Yousefi, J. Jia and J.-K. Kim, *Carbon*, 2014, **66**, 84–92.
14 S.-C. Zhang, Y. Hou, S.-M. Chen, Z. He, Z.-Y. Wang, Y. Zhu, H. Wu, H.-L. Gao and S.-H. Yu, *Adv. Mater.*, 2024, **36**, 2405682.
15 K. W. Putz, O. C. Compton, C. Segar, Z. An, S. T. Nguyen and L. C. Brinson, *ACS Nano*, 2011, **5**, 6601–6609.
16 J. Yang, M. Li, S. Fang, Y. Wang, H. He, C. Wang, Z. Zhang, B. Yuan, L. Jiang, R. H. Baughman and Q. Cheng, *Science*, 2024, **383**, 771–777.
17 H. Li, J. Zhao, L. Huang, P. Xia, Y. Zhou, J. Wang and L. Jiang, *ACS Nano*, 2022, **16**, 6224–6232.
18 H. Cheng, F. Zhao, J. Xue, G. Shi, L. Jiang and L. Qu, *ACS Nano*, 2016, **10**, 9529–9535.
19 L. Huang, H. Wu, L. Ding, J. Caro and H. Wang, *Angew. Chem., Int. Ed.*, 2024, **63**, e202314638.
20 J. Zhang, S. Uzun, S. Seyedin, P. A. Lynch, B. Akuzum, Z. Wang, S. Qin, M. Alhabeb, C. E. Shuck, W. Lei, E. C. Kumbur, W. Yang, X. Wang, G. Dion, J. M. Razal and Y. Gogotsi, *ACS Cent. Sci.*, 2020, **6**, 254–265.
21 J. Zhong, W. Sun, Q. Wei, X. Qian, H.-M. Cheng and W. Ren, *Nat. Commun.*, 2018, **9**, 3484.
22 C. Zhao, P. Zhang, J. Zhou, S. Qi, Y. Yamauchi, R. Shi, R. Fang, Y. Ishida, S. Wang, A. P. Tomsia, M. Liu and L. Jiang, *Nature*, 2020, **580**, 210–215.
23 G. Xin, W. Zhu, Y. Deng, J. Cheng, L. T. Zhang, A. J. Chung, S. De and J. Lian, *Nat. Nanotechnol.*, 2019, **14**, 168–175.
24 H. Tu, K. Xie, X. Lin, R. Zhang, F. Chen, Q. Fu, B. Duan and L. Zhang, *J. Mater. Chem. A*, 2021, **9**, 10304–10315.
25 P. Li, M. Yang, Y. Liu, H. Qin, J. Liu, Z. Xu, Y. Liu, F. Meng, J. Lin, F. Wang and C. Gao, *Nat. Commun.*, 2020, **11**, 2645.

26 S. Wan, Y. Chen, S. Fang, S. Wang, Z. Xu, L. Jiang, R. H. Baughman and Q. Cheng, *Nat. Mater.*, 2021, **20**, 624–631.
27 S. Wan, X. Li, Y. Wang, Y. Chen, X. Xie, R. Yang, A. P. Tomsia, L. Jiang and Q. Cheng, *Proc. Natl. Acad. Sci. U. S. A.*, 2020, **117**, 27154–27161.
28 X. Jiang, L. Zhang, Y. Miao, L. Chen, J. Liu, T. Zhang, S. Cheng, Y. Song and Y. Zhao, *Water Res.*, 2025, **276**, 123291.
29 Y. Miao, Y. Zhao, L. Zhang, L. Chen, R. Gao, X. Jiang, S. Song and T. Zhang, *J. Colloid Interface Sci.*, 2023, **652**, 1620–1630.
30 T. Wen, Y. Zhao, X. Wang, L. Chen, R. Gao, S. Wang and T. Zhang, *Chem. Eng. J.*, 2023, **475**, 146101.
31 L. Cao, H. Wu, P. Yang, X. He, J. Li, Y. Li, M. Xu, M. Qiu and Z. Jiang, *Adv. Funct. Mater.*, 2018, **28**, 1804944.
32 Y.-Q. Li, T. Yu, T.-Y. Yang, L.-X. Zheng and K. Liao, *Adv. Mater.*, 2012, **24**, 3426–3431.
33 P. Yang, H. Wu, N. A. Khan, B. Shi, X. He, L. Cao, X. Mao, R. Zhao, M. Qiu and Z. Jiang, *J. Membr. Sci.*, 2020, **606**, 118136.
34 J. Chen, Z. Shen, Q. Kang, X. Qian, S. Li, P. Jiang and X. Huang, *Sci. Bull.*, 2022, **67**, 609–618.
35 T. Zhang, B. Ren, H. Bai, T. Wen, L. Chen, S. Ma, X. Wang, S. Wang and Y. Zhao, *J. Membr. Sci.*, 2023, **675**, 121573.
36 S. Qin, D. Liu, G. Wang, D. Portehault, C. J. Garvey, Y. Gogotsi, W. Lei and Y. Chen, *J. Am. Chem. Soc.*, 2017, **139**, 6314–6320.
37 Z. Li, W. Wang, Y. Chen, C. Xiong, G. He, Y. Cao, H. Wu, M. D. Guiver and Z. Jiang, *J. Mater. Chem. A*, 2016, **4**, 2340–2348.
38 X. He, Y. Yang, H. Wu, G. He, Z. Xu, Y. Kong, L. Cao, B. Shi, Z. Zhang, C. Tongsh, K. Jiao, K. Zhu and Z. Jiang, *Adv. Mater.*, 2020, **32**, 2001284.
39 K.-D. Kreuer, S. J. Paddison, E. Spohr and M. Schuster, *Chem. Rev.*, 2004, **104**, 4637–4678.
40 Y. Jiang, Y. Wang, Z. Xu and C. Gao, *Acc. Mater. Res.*, 2020, **1**, 175–187.